EULER-LAGRANGE NUMERICAL SIMULATION OF A KEROSENE DROPLET MIST IGNITION IN AIR USING ANALYTICALLY REDUCED CHEMISTRY

A. Pestre*, T. Lesaffre*, Q. Cazères*, E. Riber* and B. Cuenot*
pestre@cerfacs.fr
*CERFACS, 42 avenue Gaspard Coriolis, TOULOUSE 31057, France

Abstract

High altitude relight is a critical aspect of the aeronautical engine certification and requires the numerical study of two-phase ignition with an accurate chemistry description. However, such configurations are stiff and may be numerically unstable. This paper provides several methods to perform two-phase ignition simulations using Analytically Reduced Chemistry (ARC) in the context of unstructured Large Eddy Simulation (LES) solver and Euler-Lagrange formalism. Firstly, an exponential formulation combined with a local and dynamic sub-cycling of the stiff chemistry is demonstrated to allow its stable integration at the flow time-step. Secondly, a particle-bursting method is applied to limit the impact of stiffness induced by the Lagrangian point-source approach in fine meshes. These methods are then applied in the simulation of ignition of a mono-disperse, multi-component kerosene spray in air. The use of the ARC model enables to describe in detail the chemical structure of the flame kernel during its formation. Moreover, local increase of fuel concentration is observed as the ignition proceeds which has a large influence on the combustion processes and the flame kernel development.

Introduction

Ignition at high altitude condition is a critical aspect of aeronautical engine certification. As evidenced by experimental measurements [1], low pressure (**P=0.3 bar**) and low temperature (**T=233 K**) conditions (labeled LPLT in the following) have a large detrimental influence on ignition. On one hand, LPLT conditions impact the chemistry of combustion, and more specifically the initiation reactions. Therefore, an accurate chemistry description is required to study these phenomena. On the other hand, LPLT conditions also influence the two-phase processes such as fuel atomization and droplet evaporation. Hence, the disperse phase must be accounted for in ignition simulations to fully understand the effect of LPLT.

Because of the strong evaporation-combustion coupling, ignition of two-phase mixtures is a very stiff process. Indeed, fuel evaporation at droplet positions initially induces very localized fuel spots which undergo endothermic pyrolysis and exothermic oxidation, themselves producing localized hot and cold spots. This finally creates very strong fluctuations of evaporation and chemical reaction rates that are difficult to handle numerically. Therefore, new numerical strategies are required for stable computations.

To this purpose several numerical strategies are proposed in this study. First, chemistry is integrated with a semi-implicit exponential formulation [2] associated to a local and dynamic sub-cycling (LDSC) procedure [3]. Then a particle-bursting method (PBM) is used to spatially re-distribute the local fuel evaporation source terms inherent to the point source assumption of the Lagrangian formalism. These methods are first presented in the following sections and then applied to the simulation of a three-dimensional two-phase ignition.

Chemistry

Chemical kinetics

The kinetic mechanism developed by the CRECK modeling group [4] has been used as reference. This detailed mechanism allows an accurate description of carbonated species combustion. The Jet-A1 aeronautical fuel kerosene is emulated using a multi-component surrogate composed of three species: 60% n-dodecane (NC12) that stands for the paraffin behavior, 20%

methyl-cyclohexane (MCYC6) representing the cyclic species and 20% xylene (XYL) for the aromatics (in volume) [5].

To be affordable in 3-dimensional simulations, the number of species and reactions, and the stiffness of the chemistry must be reduced [6]. This is achieved here with the software ARCANE [7] which automatically and successively applies reduction techniques. Firstly, unnecessary species and reactions are discarded using DRGEP method [8] to obtain a skeletal mechanism. The ARC mechanism is finally obtained by applying the Quasi-Steady-State Approximation (QSS) [9]. Under this assumption, species with a very short characteristic timescale are considered to have zero net chemical source term, leading to algebraic expressions for their concentration. Therefore, there is no need to solve their conservation equation, which drastically reduces the numerical cost and the chemical stiffness.

The chemical reduction is performed based on the following test cases: a) 1-dimensional premixed flames at LPLT conditions, targeting the laminar flame speed, the adiabatic temperature and species concentrations of the main products (CO2, H2O and CO); b) 0-dimensional constant pressure reactors at low pressure to verify the auto-ignition time. The resulting ARC mechanism is composed of 30 transported species, 299 reactions, 22 QSS species and is labeled S30R299QSS22 in the following. Validation profiles are given on Fig. 1 showing the laminar flame speed versus equivalence ratio and auto-ignition time versus initial temperature. A very good agreement is obtained with detailed CRECK mechanism. Note that this reduced chemistry has been also evaluated in gaseous forced ignition configurations [3].

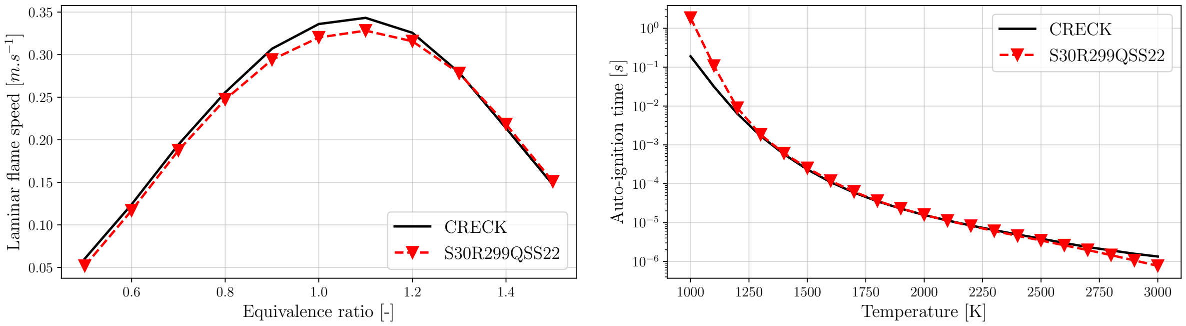

Figure 1: Comparison of ARC scheme (S30R299QSS22) with the reference detailed scheme (CRECK) for: laminar flame speed versus equivalence ratio in a 1-dimensional premixed flame at P=0.3 bar and T=233 K (left) and auto-ignition time versus initial temperature in a 0-dimensional constant pressure reactor with stoichiometric mixture at P=0.3 bar (right).

Chemistry integration

To avoid the high numerical cost induced by the explicit integration of stiff ARC mechanisms, the exponential integration method [2] is used and summarized below. The species are assumed to be produced or consumed following a first order differential equation:

$$\frac{dc_k}{dt} = \dot{\omega}_k = A_k c_k + B_k \tag{1}$$

where c_k is the concentration of species k and $\dot{\omega}_k$ the species production rate which can be decomposed into $A_k c_k$ and B_k the contributions to destruction and creation respectively. The analytical solution is known and can be written in discretized form as:

$$c_k^{n+1} = c_k^n + \frac{B_k^n}{A_k^n} \exp(A_k^n \Delta t) - \frac{B_k^n}{A_k^n} \tag{2}$$

where n and $n+1$ are successive iterations.

$$A_k c_k = \sum_{j=1}^{N_{reac}} \dot{\omega}_{k,j} \text{ for all } \dot{\omega}_{k,j} < 0 \quad ; \quad B_k = \sum_{j=1}^{N_{reac}} \dot{\omega}_{k,j} \text{ for all } \dot{\omega}_{k,j} > 0 \tag{3}$$

where N_{reac} is the total number of reactions in the ARC mechanism and $\dot{\omega}_{k,j}$ is the chemical rate of species k associated to reaction j and is computed with Arrhenius laws.

In addition, a local and dynamic sub-cycling procedure (LDSC) is applied to the computation of the chemical source terms [3]. The current time-step of the computation (Δt) is divided into smaller time-steps ($\Delta t_{chem-SC} = \Delta t / N_{Sub-Cyc}$) for the chemistry integration. The number of sub-cycles $N_{Sub-Cyc}$ is determined locally and at each iteration based on chemical time scales approximated by the inverse of species production rates. For each species, the maximum allowed time step corresponds to 1% variation of the species concentrations:

$$\Delta t_{chem,k} = \frac{c_k}{\dot{\omega}_k} \times 0.01 \tag{4}$$

In this study, the number of sub-cycles observed in reactive zones is of the order of one hundred and can reach five hundreds for highly reactive unstable regions.

The exponential integration method associated to the LDSC have been evaluated on gaseous ignition configurations and have demonstrated their efficiency [3]. These methods enable to use large flow time-steps with ARC chemistries up to the acoustic CFL (Courant-Friedrichs-Lewy) and Fourier limits required by the compressible solver, without compromising the accuracy. Therefore, they largely reduce the computational cost of 3-dimensional computations.

Two-phase flow

Discrete Multi-Component evaporation model

The multi-component surrogate model for Jet-A1 also impacts evaporation. In this study a Discrete Multi-Component (DMC) evaporation model based on the Spalding model [10] is used and briefly recalled here. The Spalding droplet evaporation rate writes:

$$\frac{dm_p}{dt} = -Sh^* \pi d_p \rho D \ln(1 + B_M) \tag{5}$$

where m_p is the mass of the particle and d_p is the particle diameter. The gaseous density ρ and the fuel species diffusivity D are estimated through the classical 1/3 rule between the droplet surface and the far field state. Sh^* is a modified Sherwood number proposed by Abramzon and Sirignano [11] to better estimate the mass flux considering the boundary layer around the droplet. Finally, the mass Spalding number B_M is computed for multi-component mixtures as:

$$B_M = \frac{\sum_{k=1}^{N_{fuel}} Y_{k,s} - \sum_{k=1}^{N_{fuel}} Y_{k,\infty}}{1 - \sum_{k=1}^{N_{fuel}} Y_{k,s}} = \frac{Y_{k,s} - Y_{k,\infty}}{\varepsilon_k - Y_{k,s}} \tag{6}$$

where $Y_{k,s}$ and $Y_{k,\infty}$ are the species mass fractions of each fuel component respectively at the droplet surface and the far field. Only the components present in the liquid phase are considered in Eq. (6). The surface mass fractions are determined with a liquid equilibrium in Eq. (7) where $P_{sat,k}$, the vapor pressure, is obtained by the Clausius-Clapeyron relation.

$$X_{k,s} P = X_{liq,k} P_{sat,k} \tag{7}$$

with P the pressure at the droplet position and $X_{liq,k}$ the liquid mole fraction of the fuel species k in the droplet. Typically, in a Lagrangian approach, the $Y_{k,\infty}$ is taken as the value in the cell containing the droplet. Using the second part of Eq. (7), the individual component fractions of vapor can be computed and $\dot{m}_{p,k}$, the individual component evaporation rates write:

$$\dot{m}_{p,k} = \varepsilon_k \dot{m}_p \tag{8}$$

The DMC evaporation model has been validated in [12].

Point source correction

The standard Lagrangian formalism uses the point source approximation, in which droplets are represented as material points transporting the droplet properties. In this approximation all source terms produced by droplets are applied to the gas in the cell containing the particle. As a consequence, when using fine meshes the droplet evaporation creates localized peaks in the Eulerian fuel species fields at the droplet position. In the case of ignition, where droplets are placed in a hot environment, the fuel vapor produced in one cell directly pyrolyse before diffusing, resulting in pointwise combustion occurring at the droplet location. This then leads to point to point strong gradient variations that are numerically difficult to handle. This problem is well known and a number of regularization methods may be found in the literature [13]. However, most methods involve surrounding cells of the droplet-containing cell, which can be very costly when computing on unstructured grid.

In this work, an alternative is proposed that stays efficient on unstructured grids. The particle bursting method (PBM) is based on the R-parcel technique which consists in computing only numerical particles which represent R_p physical particles, instead of computing directly the R_p physical particles [14]. This R-parcel concept was originally introduced to decrease the computational cost of Euler-Lagrange simulations by taking $R_p > 1$. It is used here with $R_p < 1$ to represent one physical particle with a cloud of numerical particles, therefore smoothing out the associated source terms. In the PBM method, the parent physical droplets are burst in N_{burst} child droplets with $R_p = 1/N_{burst}$. These child droplets are randomly dispersed in a control volume around the initial parent droplet position and form localized droplet clusters. The child numerical particles have the same mass, temperature and radii than the physical one and thus follow the same evaporation model. However, the mass and heat fluxes transmitted to the gaseous phase are weighted by R_p to ensure mass, momentum and energy conservation. Since the child droplets are dispersed around the physical one, all source terms are automatically spread in the control volume as illustrated in Fig. 2. In this study, the control volume is a sphere of radius $R_c = 2\Delta x$ and $N_{burst} = 100$ to ensure a homogeneous repartition.

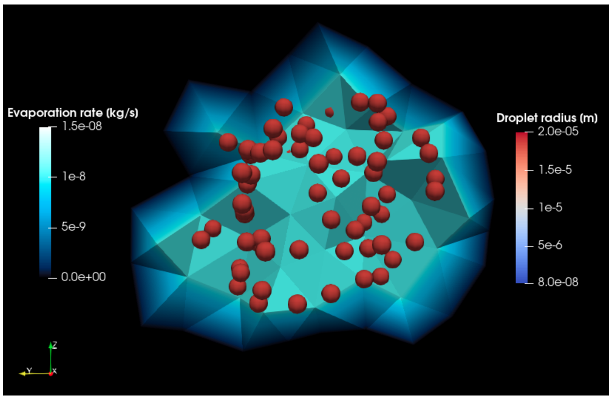

Figure 2: Illustration of the PBM resulting droplet cluster with the corresponding evaporation rate field.

3D Configuration

Two-phase ignition in a spherical bomb is considered and sketched on Fig. 3. The domain radius is $5\,cm$, yet, only the center, where combustion processes occur, is refined with a characteristic grid size $\Delta x = 100\,\mu m$ which ensures at least 10 points in the flame front. Thus, no combustion models are required. The resulting unstructured mesh is composed of 4.61 million elements.

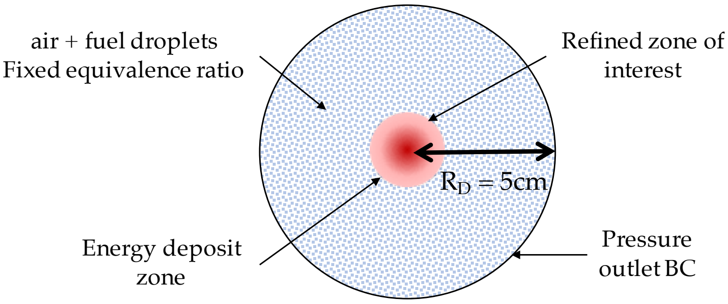

Figure 3: Spherical bomb ignition configuration.

The domain is initially filled with a stoichiometric mixture of droplets in air ($\phi_{g,0} = 0$ and $\phi_{tot,0} = \phi_{l,0} = 1$ where $\phi_{tot,0}$, $\phi_{g,0}$ and $\phi_{l,0}$ are respectively the total, gaseous and liquid initial equivalence ratios) at rest and at high altitude conditions ($P = 0.3\,bar, T = 233\,K$). The liquid phase is homogeneously distributed with single-size droplets diameter of initially $d_p = 10\,\mu m$. The droplet temperature is initially equal to the gaseous temperature.

Non-reflecting pressure outlet boundary conditions are applied with the Navier-Stokes Characteristic Boundary Conditions formalism [15] to maintain a constant pressure in the domain and to evacuate the pressure wave created at ignition.

The ignition is triggered with an energy deposit at the center of the domain. The energy deposit model [16] corresponds to a source term E_s applied to the energy equation, and writes:

$$E_s(x,y,z,t) = \frac{\epsilon_i}{(4\pi)^2 \sigma_t \sigma_s^3} \exp\left(\frac{(t-t_0)^2}{2\sigma_t^2}\right) \exp\left(\frac{(x-x_0)^2 + (y-y_0)^2 + (z-z_0)^2}{2\sigma_s^2}\right) \quad (9)$$

with $\epsilon_i = 200\,mJ$ the total deposited energy chosen to reach a maximum temperature of $3000\,K$ during the deposit. The coordinates (x_0, y_0, z_0) correspond to the center of the deposit volume, and $t_0 = 50\,\mu s$ is the time of maximum energy deposition. Finally, σ_s and σ_t are the characteristic size and duration of the deposit respectively, and are derived from the Gaussian distribution so as to reach at a distance $\Delta_{s,t}$ an amplitude of one thousandth of the amplitude at the deposition center:

$$\Delta_{s,t} = \sigma_{s,t} \times \sqrt{2\ln(10^4)} \quad (10)$$

For this study the deposition duration is $2\Delta_t = 100\,\mu s$, and the radius is $\Delta_s = 2\,cm$.

The computation is performed with the AVBP code (`https://www.cerfacs.fr/avbp7x/`) which solves the reactive and compressible Navier-Stokes flow equations with a central finite volume Lax-Wendroff scheme, second order both in time and space [17]. The dispersed phase is solved using the Lagrangian formalism. Source terms of mass, momentum and energy from the liquid to gaseous phase are distributed to the closest nodes in the Eulerian grid in a two-way coupling approach.

Results

Overview

The temporal evolutions of maximum temperature and mean heat release rate weighted by the cell volume are displayed on Fig. 4. There is a first endothermic ignition phase at $t = 70\,\mu s$ quickly followed by a large increase of heat release rate at $t = 90\,\mu s$ which corresponds to the oxidation processes and leads to the flame front formation. Then, the heat release rate stabilizes at a much lower value corresponding to a flame propagation mode. The kernel maximum temperature also stabilizes around $T_{max} = 2000\,K$ after the end of the energy deposit, which indicates an ignition success.

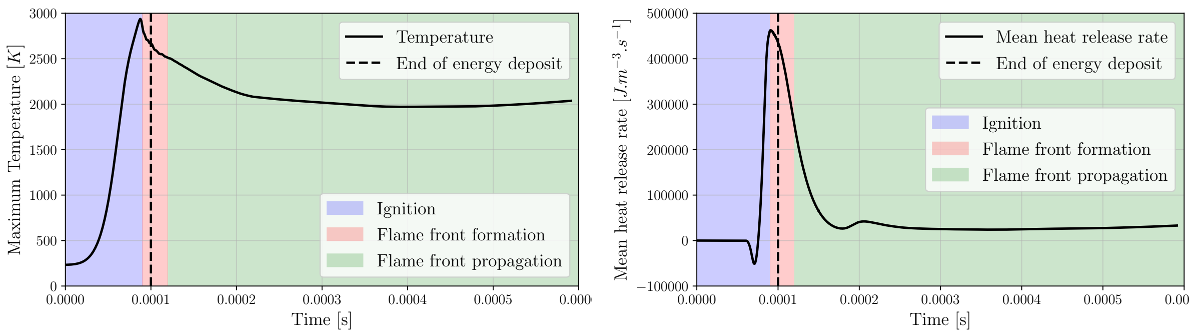

Figure 4: Temporal evolutions of maximum temperature and mean heat release rate.

In the following sections the two-phase combustion mechanisms are detailed for the three ignition phases: (i) until $t = 90\,\mu s$, early ignition, (ii) until $t = 120\,\mu s$, flame front formation, and (iii) until $t = 600\,\mu s$, flame front propagation.

Early ignition phase

The energy deposit heats the gas, which then heats the droplets through conduction. Evaporation starts when the droplet temperature is high enough, and is therefore strongest at the deposit center where the temperature is highest, as shown on Fig. 5. Due to the small droplet characteristic size, the droplet density is high and the resulting evaporation rate field projected on the Eulerian grid is quite smooth, and only few empty spots appear. The gaseous equivalence ratio (computed from the atomic balance of carbon, hydrogen and oxygen) increases accordingly and exceeds stoichiometry at the kernel center where combustion can then start. Note that the equivalence ratio is more sensitive to the liquid phase discrete distribution and does not appear as smooth as evaporation because of diffusion effects towards empty evaporation regions. These regions are highlighted with the iso-surfaces on Fig. 5 (right) delimiting the no-evaporation zones in a thickness of $8\Delta x$ centered on the cut-plane. These regions are well correlated with the fluctuations of equivalence ratio.

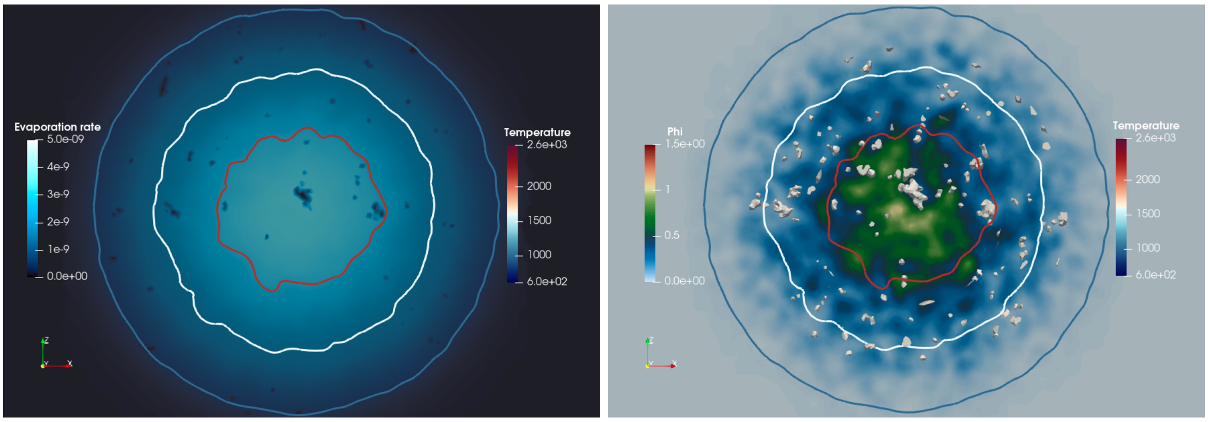

Figure 5: Evaporation rate (left) and equivalence ratio (right) cut-plane fields with temperature iso-contours of $T = 1000\,K, 1600\,K$ and $2200\,K$, at $t = 80\,\mu s$. The iso-surfaces on the right picture correspond to the no-evaporation zones in a thickness of $8\Delta x$ centered on the cut-plane.

Combustion indeed starts at the kernel center as shown on Fig. 6, in a mixed reactor combustion regime, meaning that the thin propagating flame front has not formed yet. This is confirmed by the pool of reactive radical species such as OH found at the center where $T > 2000\,K$. Interestingly, this flame kernel is bordered by a spherical endothermic zone around $T = 1600\,K$. This endothermic process corresponds to fuel pyrolysis, which occurs everywhere in the reaction zone but is not masked by exothermic combustion only in the lower temperature region. This is well evidenced by the field of nC_7H_{14} species which is the first pyrolysis product of the fuel component MCYC6: although produced everywhere in the reaction zone, nC_7H_{14} only appears at the border where it is not consumed by oxidation reactions.

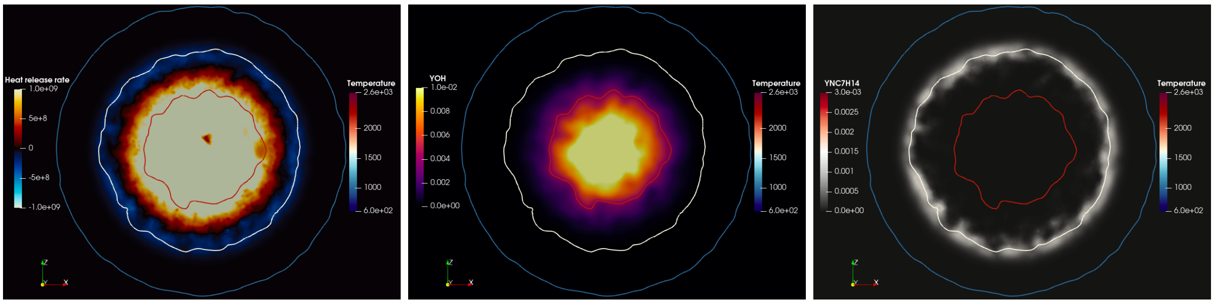

Figure 6: Heat release rate (left), OH mass fraction (center) and nC_7H_{14} mass fraction (right) cut-plane fields with temperature iso-contours of $T = 1000\,K, 1600\,K$ and $2200\,K$, at $t = 80\,\mu s$.

The fuel components mass fraction fields displayed on Fig. 7 well illustrate preferential evaporation where MCYC6 being the most volatile species evaporates first as soon as T reaches $1000\,K$. In the hottest center zone where $T > 1600\,K$, this species is immediately pyrolyzed after evaporation and thus disappears. The same mechanism applies to XYL but this less volatile species requires a higher temperature to evaporate and is found only above $\sim 1500\,K$. Finally, a negligible quantity of NC12 is observed in the domain (not shown) because the droplet temperature is still too low at that time to enable its evaporation. Indeed, Fig. 8 indicates that this species has not started to evaporate at the end of the early ignition phase ($t = 90\,\mu s$). This means that this phase is totally driven by MCYC6 and XYL, which is a major difference with gaseous ignition of the same fuel blend where NC12 would pyrolyse simultaneously with the other components [18].

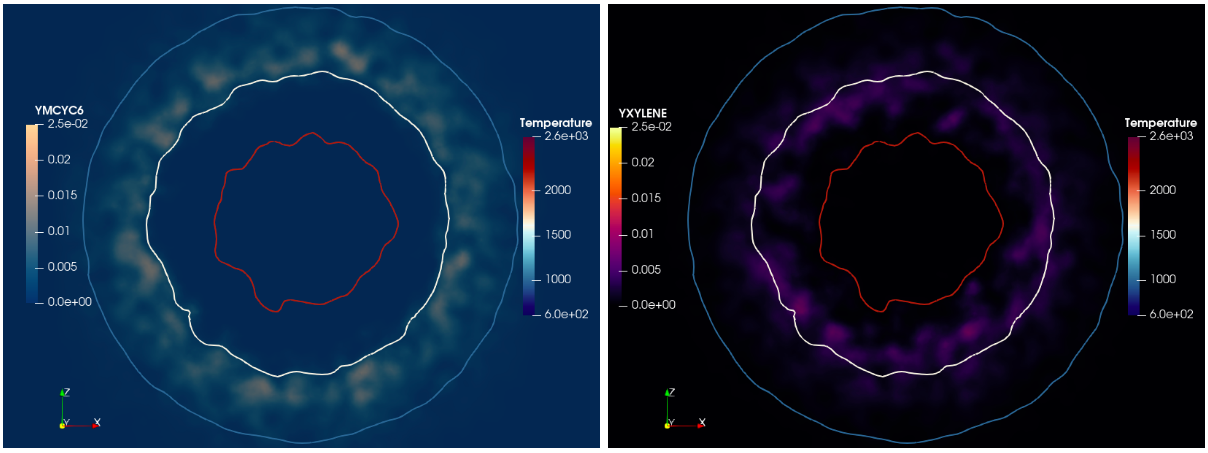

Figure 7: MCYC6 mass fraction (left) and XYL mass fraction (right) cut-plane fields with temperature iso-contours of $T = 1000\,K, 1600\,K$ and $2200\,K$, at $t = 80\,\mu s$.

Combustion in this early ignition phase has not much progressed even at the kernel center, where the concentrations of the main combustion products CO, CO_2 and H_2O are still low and the oxidizer O_2 has been barely consumed.

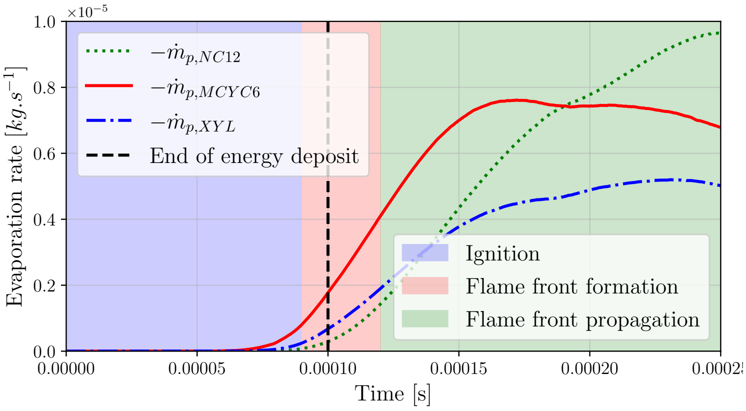

Figure 8: Temporal evolution of the fuel component evaporation rates during the early ignition phase.

Flame front formation
After the ignition phase at $t = 100\,\mu s$, a propagating flame front has formed as shown on Fig. 9 with the heat release rate and the radical species OH and CH_2O. The flame front is located around the iso-contour $T = 1600\,K$ which corresponds to the critical temperature for fuel pyrolysis.

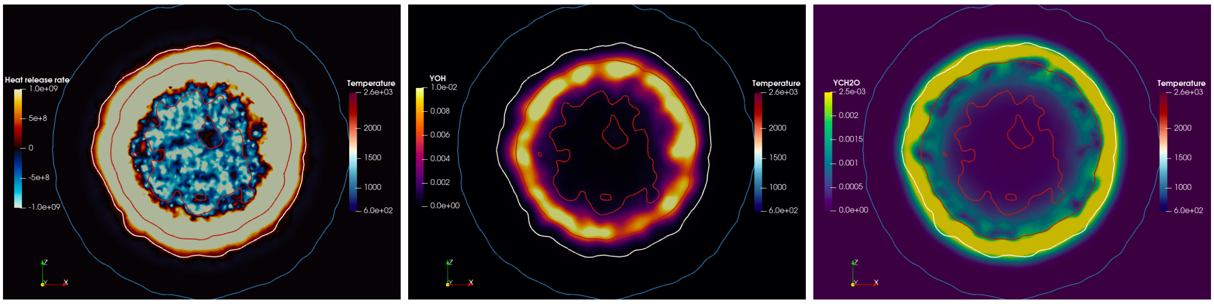

Figure 9: Heat release rate (left), OH mass fraction (center) and CH_2O mass fraction (right) cut-plane fields with temperature iso-contours of $T = 1000\,K$, $1600\,K$ and $2200\,K$, at $t = 100\,\mu s$.

Similarly to the previous phase, fuel component vapor is visible along the reaction zone in the low temperature side, but this time NC12 has started to evaporate and is present, in much less proportion, about ten time smaller than MCYC6 and XYL (see Fig. 10). Hence again at this stage, the flame properties are mainly driven by these two fuel components.

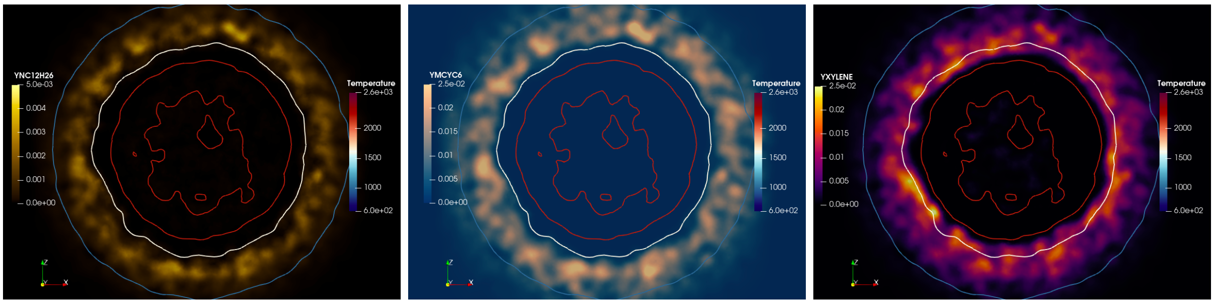

Figure 10: NC12 (left), MCYC6 (center) and XYL (right) mass fraction cut-plane fields with temperature iso-contours of $T = 1000\,K$, $1600\,K$ and $2200\,K$, at $t = 100\,\mu s$.

As shown on Fig. 11 (right), the flame front propagates in a mixture around stoichiometry. The two-phase combustion regime is of the kind of weakly evaporation-controlled where the gaseous mixture has reached flammability before reaching the flame [19]. Therefore, the flame front propagation is not controlled by the droplet evaporation. The weakly controlled evaporation regime is characterized in laminar propagating flames by an evaporation peak located ahead of the flame front in the fresh gases. The situation is different in sparked ignition, where the droplet evaporation is triggered by the energy deposition rather than the flame front. Therefore, the peak evaporation is not located in the fresh gases but remains at the kernel center, until all droplets have evaporated, inducing there large values of the equivalence ratio as shown on Fig.11

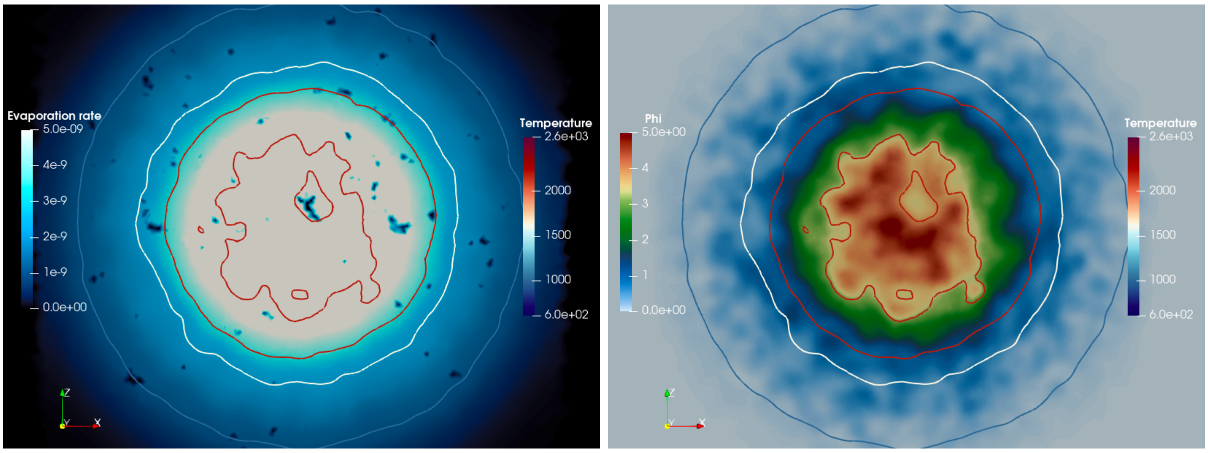

Figure 11: Evaporation rate (left) and equivalence ratio (right) cut-plane fields with temperature iso-contours of $T = 1000\,K$, 1600 K and 2200 K, at $t = 100\,\mu s$.

The evaporated fuel components that evaporate inside the volume enclosed by the flame pyrolyze immediately, leading to the formation of light carbonated species such as CH_3 and C_2H_2 (see Fig. 12). These carbonated species however do not oxidize due to the lack of oxygenated species. Therefore, the temperature is reduced at the kernel center due to both evaporation and pyrolysis. The formation of such rich, not flammable and cooler mixture at the center may be detrimental for the kernel survival and ultimately endanger the ignition process.

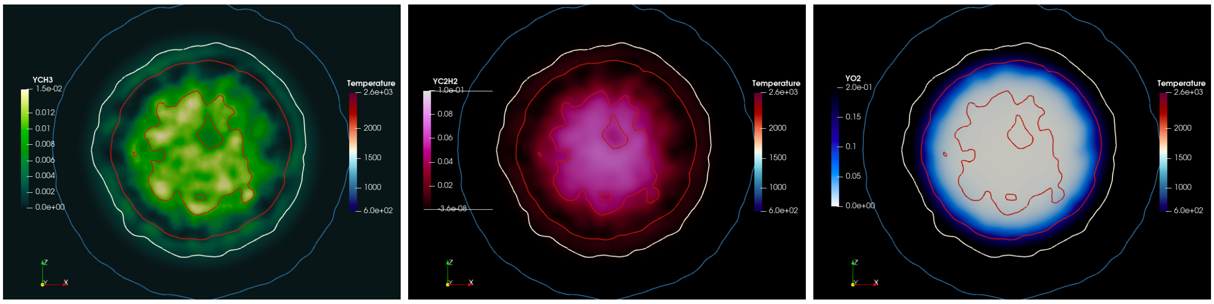

Figure 12: CH_3 (left), C_2H_2 (center) and O_2 (right) mass fraction cut-plane fields with temperature iso-contours of $T = 1000\,K$, 1600 K and 2200 K, at $t = 100\,\mu s$.

The number of droplets was initially set to obtain a stoichiometric total equivalence ratio, computed from the mixing with cold air before energy deposit. Since the pressure is constant in the domain, the temperature increase resulting from the energy deposit induces a local decrease of the gas density and an expanding radial flow, which both reduce the oxidizer mass content. Therefore, the two-phase mixture becomes rich and when the droplets start to evaporate, there are fewer oxygen atoms in the gas phase than initially targeted. The resulting total equivalence ratio can be estimated by correcting the initial value with the gas expansion effect as in Eq. (11), which gives the maximum value which can be reached:

$$\phi^*_{tot,max} = \phi_{g,0} + \phi_{l,0} \times \frac{\rho_0}{\rho_{min}} \tag{11}$$

where $\phi^*_{tot,max}$ is the rescaled total equivalence ratio before ignition, $\phi_{g,0}$ and $\phi_{l,0}$ are respectively the initial gaseous and liquid components of the equivalence ratio and ρ_{min} and ρ_0 are respectively the minimum and initial gaseous densities. In the present case, the theoretical value $\phi^*_{tot,max} = 12.5$ is never reached as it assumes to conserve the same minimum density during the entire evaporation. At the end of the evaporation, the value $\phi_{tot,max} = 8.5$ is observed.

Finally, the main combustion products are presented on Fig. 13. A large amount of CO is released whereas the CO_2 production is limited which is characteristic of rich combustion processes. Furthermore, a small depletion of H_2O and CO_2 is observed at the kernel center where the equivalence ratio is the highest. The formation of combustion products and the complete consumption of oxidizer at the kernel center indicate that the combustion is complete at the kernel center. This is also confirmed on Fig. 9 where there is no exothermic heat release rate or oxidized radicals at the kernel center.

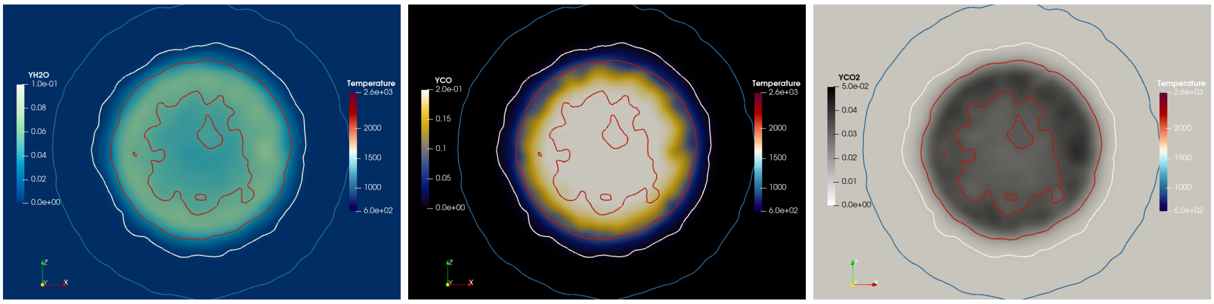

Figure 13: H_2O (left),CO (center) and CO_2 (right) mass fraction cut-plane fields with temperature iso-contours of $T = 1000\,K$, $1600\,K$ and $2200\,K$, at $t = 100\,\mu s$.

Figure 14 shows the temporal evolution of the smallest droplet radius, which is located at the kernel center. At the end of the flame formation phase ($t = 100\,\mu s$) the droplet radius has been reduced by only 15 percent, which means that evaporation may continue in the next phase. At this time however energy deposition stops and the required heat for evaporation will be now taken from the gas. This may lead to either ignition success or failure, depending on the energy balance of the hot gas.

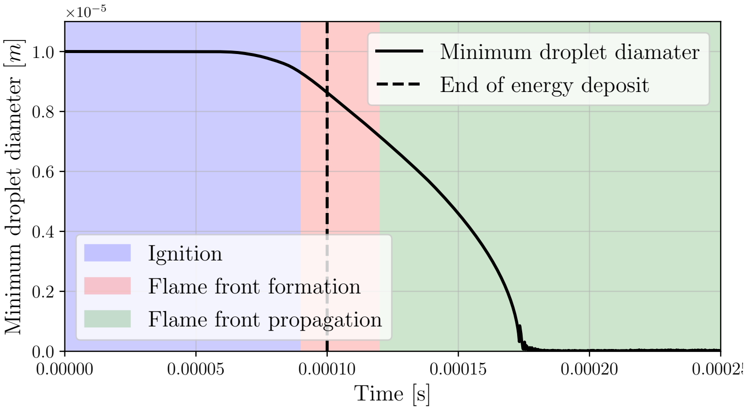

Figure 14: Temporal evolution of the smallest droplet radius.

Flame front propagation
Jumping to much later time ($t = 500\,\mu s$) a propagating flame is observed, meaning a successful ignition (see Fig. 15). Because energy deposition has stopped, the hot gas temperature has decreased slightly below 2000K but stabilizes there. As may be seen from Fig. 14, droplets completed evaporation in the hot gas region at around $t = 175\,\mu s$. Thus at $t = 500\,\mu s$ all endothermic processes have also completed. However, the resulting very high equivalence ratio, up to 5, does not allow oxidation of the pyrolysis products in this hot zone.

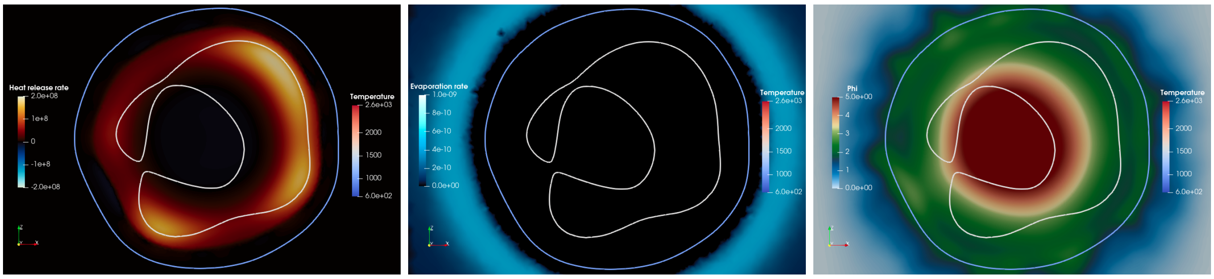

Figure 15: Heat release rate (left), evaporation rate (center) and equivalence ratio (right) cut-plane fields with temperature iso-contours of $T = 1000\,K$, $1600\,K$ and $2200\,K$, at $t = 500\,\mu s$.

Figure 15 (center) shows that evaporation now only occurs in a spherical zone around the flame front on the cold air side. This means that evaporation is fast enough in the pre-heat zone to feed the propagating flame, which has become therefore purely gaseous. The evaporation zone lies much further from the hot gas than the flame front because evaporation starts at low droplet temperature ($T_p \approx 450 - 500\,K$) compared to the gas temperature at the flame front location ($T = 1600\,K$).

Finally, due to the high equivalence ratio resulting from the complete evaporation, the flame evolves in a very rich mixture at the flammability limit ($\phi \approx 2 - 3$). At this equivalence ratio, the flame is thick and propagates slowly. This reflects on the maximum heat release rate which is one order magnitude lower than it was in the previous phase (see Fig. 9). This too rich fresh mixture is therefore detrimental for the kernel development and may lead ultimately to extinction. In practice however the turbulent flow may counteract this effect by promoting mixing with fresh air in the pre-heat zone and lowering the too high equivalence ratio.

Conclusion

Thanks to numerical stabilization methods for stiff problems, namely exponential chemistry integration, local and dynamic sub-cycling (LDSC) and particle bursting (PBM), the ignition simulation of a mono-disperse, multi-component kerosene droplet cloud was performed. Accurate chemistry was described with an ARC scheme. In particular the interest of the PBM was demonstrated, allowing to reduce the evaporation rate source term stiffness associated to the point source approximation. However, the PBM still requires further study to define suitable physical criteria to determine the control volume size and the number of child particles, which also depend on the parent droplet diameter and the mesh discretization respectively.

Results clearly highlighted preferential evaporation effects on ignition in two-phase mixtures, with a dominant role of the most volatile species (methyl-cyclohexane and xylene) in the early phases. Due to the high droplet number density, all two-phase fields appeared quite homogeneous and the flame was weakly perturbed by the dispersed phase. The ARC scheme allowed to describe the endothermic pyrolysis of the fuel components, which was also found to play a role in the ignition scenario. Another important observed behavior was the evolution of the equivalence ratio toward very rich values, due to the decrease of oxygen content associated to the density decrease when the gas heats up, while the fuel content in the droplets does not change. This led eventually to a very rich propagating flame, which may endanger the full ignition process. At the end of the simulated sequence, a two-phase flame is obtained which propagates in a purely gaseous mixture as droplets fully evaporate ahead of the reacting zone.

The developed numerical methodology allows now to consider other and more complex cases, including poly-disperse effects with a realistic spray distribution, turbulence and influence of high-altitude conditions.

References

[1] Martinos, A., Zarzalis, N., Harth, S., “Analysis of ignition processes at combustors for aero engines at high altitude conditions”, in *Proc ASME Turbo Expo 2020* (2020).

[2] Blanchard, S., Cuenot, B., Cazeres, Q., “Chemical modelling for methane oxy-combustion in Liquid Rocket Engines”, *Acta Astronautica* 190: 98–111 (2022).

[3] Pestre, A., Cuenot, B., Riber, E., “Evaluation of numerical methods for explicit chemistry integration and application on DNS of turbulent kerosene ignition at high altitude conditions”, in *Proc 10th European Combustion Meeting* (2021).

[4] Ranzi, E., Frassoldati, A., Stagni, A., Pelucchi, M., Cuoci, A., Faravelli, T., “Reduced kinetic schemes of complex reaction systems: Fossil and biomass-derived transportation fuels”, *International Journal of Chemical Kinetics* 46: 512–542 (2014).

[5] Humer, S., Seiser, R., Seshadri, K., “Experimental investigation of combustion of jet fuels and surrogates in nonpremixed flows”, *Journal of Propulsion and Power* 27 (2011).

[6] Lu, T., Law, C., Yoo, C., Chen, J., “Dynamic stiffness removal for direct numerical simulations”, *Combustion and Flame* 156: 1542–1551 (2009).

[7] Cazères, Q., Pepiot-Desjardins, P., Riber, E., Cuenot, B., “A fully automatic procedure for the analytical reduction of chemical kinetics mechanisms for Computational Fluid Dynamics applications”, *FUEL* 303 (2021).

[8] Pepiot-Desjardins, P., Pitsch, H., “An efficient error-propagation-based reduction method for large chemical kinetic mechanisms”, *Combustion and Flame* 154: 67–81 (2008).

[9] Lu, T., Law, C., “Systematic approach to obtain analytic solutions of quasi steady state species in reduced mechanisms”, *Journal of Phys. Chem. A.* 110: 13202–13208 (2006).

[10] Spalding, D., “The combustion of liquid fuels”, *Symposium (International) on Combustion* 4: 843–864 (1953).

[11] Abramzon, B., Sirignano, W., “Droplet vaporization model for spray combustion calculations”, *International Journal of Heat and Mass Transfer* 32: 1605–1618 (1989).

[12] Shastry, V., Cazères, Q., Rochette, B., Riber, E., Cuenot, B., “Numerical study of multicomponent spray flame propagation”, *Proc. of the Comb. Inst* 38: 3201–3211 (2021).

[13] Poustis, J., Senoner, J., Zuzio, D., Villedieu, P., “Regularization of the Lagrangian point force approximation for deterministic discrete particle simulations”, *International Journal of Multiphase Flow* 35: 376–388 (2009).

[14] Dukowicz, J., “A particle-fluid numerical model for liquid sprays”, *Journal of Computational Physics* 32: 229–253 (1980).

[15] Poinsot, T., Lelef, S., “Boundary conditions for direct simulations of compressible viscous flows”, *Journal of Computational Physics* 101: 104–109 (1992).

[16] Lacaze, G., Richardson, E., Poinsot, T., “Large eddy simulation of spark ignition in a turbulent methane jet”, *Combustion and Flame* 159: 1993–2009 (2009).

[17] Lax, P., Wendroff, B., “Systems of conservation laws”, *Communications on Pure and Applied Mathematics* 13: 217–227 (1960).

[18] Stagni, A., Esclapez, L., Govindaraju, P., Cuoci, A., Faravelli, T., Ihme, M., “The role of preferential evaporation on the ignition of multicomponent fuels in a homogeneous spray/air mixture”, *Proc. of the Comb. Inst* 36: 2483–2491 (2017).

[19] Rochette, B., Riber, E., Cuenot, B., “Effect of non-zero relative velocity on the flame speed of two-phase laminar flames”, *Proc. of the Comb. Inst* 37: 3393–3400 (2019).